ChemComm

COMMUNICATION

View Article Online
View Journal | View Issue

Cite this: *Chem. Commun.*, 2025, **61**, 5027

Received 10th February 2025,
Accepted 4th March 2025

DOI: 10.1039/d5cc00685f

rsc.li/chemcomm

An ultra-stable prelithiated Sn anode for sulfide-based all-solid-state Li batteries†

Haozhe Geng,[ab] Senhe Huang,[bc] Zhenyu Zhang,*[de] Sheng Han,*[a] Rongrong Miao,[f] Jinhui Zhu*[b] and Xiaodong Zhuang[bc]

A prelithiated Sn (LiSn) anode was developed for sulfide-based all-solid-state Li batteries (ASSLBs), demonstrating high compatibility with Li_6PS_5Cl sulfide electrolyte. The LiSn|NCM811 cell achieved 163 mA h g^{-1} capacity (0.1C) and 91% retention after 650 cycles (1C). Prelithiation compensated Li loss and mitigated volume expansion, enabling high-performance ASSLBs.

Compared to current commercial Li-ion batteries (LIBs), next-generation all-solid-state Li batteries (ASSLBs) offer higher energy density and enhanced safety due to the use of high-capacity Li metal anodes (LMAs) and the elimination of hazardous liquid electrolytes.[1] As a crucial component of ASSLBs, solid electrolytes (SEs) can be classified into polymers, sulfides, oxides, and halides.[2] Among these, sulfide SEs have garnered the most attention due to their exceptionally high room-temperature ionic conductivity and mechanical deformability.[3] However, sulfide-based ASSLBs suffer from severe interfacial challenges, particularly the incompatibility between LMAs and sulfide SEs.[4,5] To address these interfacial issues, alloy anodes have been explored as potential replacements for LMAs, drawing inspiration from similar strategies used to mitigate interfacial problems in LIBs.[6]

In particular, Si-based anodes have attracted significant interest for sulfide-based ASSLBs due to their high specific capacity, low voltage plateau, and good compatibility with sulfide SEs.[7,8] However, intrinsic challenges such as low electronic conductivity and large volume expansion (>300%) remain significant obstacles, leading to poor rate capability and cycling stability.[7] As an alternative, Sn-based anodes offer promising advantages. As a main-group element similar to Si, Sn exhibits significantly higher electrical conductivity (9.2×10^6 *vs.* 4.3×10^{-4} S m^{-1}) and can accommodate a large amount of Li (forming $Li_{4.4}Sn$), making it an attractive candidate for sulfide-based ASSLBs.[9] However, to achieve high-performance Sn-based sulfide ASSLBs, the associated volume expansion issue must be addressed, and the compatibility between Sn and sulfide SEs requires further investigation.

Prelithiation is a well-established strategy to enhance the electrochemical performance of alloy anodes. It not only compensates for Li loss during cycling but also mitigates volume expansion, thereby improving Coulombic efficiency (CE) and cycling stability.[10,11] Based on this approach, we synthesized a prelithiated Sn alloy (LiSn) anode by mixing and pressing Li and Sn powders. As expected, the full cell comprising a LiSn anode, Li_6PS_5Cl (LPSC) SE (Fig. S1, ESI†), and a $LiNbO_3$-coated single-crystal $LiNi_{0.8}Co_{0.1}Mn_{0.1}O_2$ (NCM811) cathode demonstrated superior electrochemical performance. It exhibited a higher specific capacity (163 *vs.* 106 *vs.* 119 mA h g^{-1} at 0.1C) and prolonged cycling stability (91% capacity retention after 650 cycles *vs.* 81% after 540 cycles *vs.* 57% after 70 cycles) compared to full cells with pure Sn anode and LMA. Further characterizations and theoretical calculations revealed that the outstanding electrochemical performance of the LiSn anode stems from its high compatibility with LPSC, along with prelithiation, which effectively compensate Li loss and alleviate volume expansion during cycling. This study introduces a highly stable Li–Sn alloy anode, expanding the range of viable anode materials for sulfide-based ASSLBs.

First, the compatibility between Li/Li alloys (*i.e.*, $Li_{22}Sn_5$, $Li_{22}Si_5$) and LPSC was evaluated using *ab initio* molecular dynamics (AIMD) simulations. Fig. 1a presents the net charges

[a] *School of Chemical and Environmental Engineering, Shanghai Institute of Technology, Shanghai 201418, China. E-mail: hansheng654321@sina.com*
[b] *The Soft2D Lab, State Key Laboratory of Metal Matrix Composites, Shanghai Key Laboratory of Electrical Insulation and Thermal Ageing, School of Chemistry and Chemical Engineering, Shanghai Jiao Tong University, Shanghai 200240, China. E-mail: zhujinhui1109@sjtu.edu.cn*
[c] *Frontiers Science Center for Transformative Molecules, Zhang Jiang Institute for Advanced Study, Shanghai Jiao Tong University, Shanghai 201203, China*
[d] *National Engineering Research Center of Light Alloy Net Forming & State Key Laboratory of Metal Matrix Composite, Shanghai Jiao Tong University, 800 Dongchuan Road, Shanghai 200240, China. E-mail: zhangzhenyu@snerdi.com.cn*
[e] *Shanghai Nuclear Engineering Research and Design Institute Co., Ltd., 169 Tianlin Road, Xuhui District, Shanghai 200030, China*
[f] *School of Chemical Engineering and Energy Technology, Dongguan University of Technology, Dongguan, 523808, China*

† Electronic supplementary information (ESI) available. See DOI: https://doi.org/10.1039/d5cc00685f

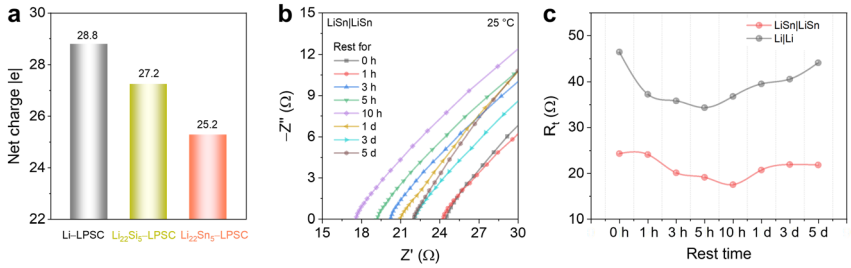

Fig. 1 (a) Net charges of Li/Li alloys and LPSC SE obtained from AIMD simulations. (b) Nyquist plots of LiSn|LiSn cells, demonstrating the evolution of cell impedance over varying rest times. (c) Changes in R_t for LiSn|LiSn and Li|Li cells as a function of rest time.

of the Li/Li alloys and LPSC SE after AIMD simulations of the anode–SE interface (Fig. S2, ESI†). A higher net charge indicates greater charge transfer, which corresponds to higher reactivity between the two components.[12] Notably, the $Li_{22}Sn_5$–SE system exhibits the lowest net charge compared to the Li–SE and $Li_{22}Si_5$–SE systems, suggesting that the Li–Sn alloy has the highest stability with LPSC SE. To further verify this stability, symmetric LiSn|LiSn and control Li|Li cells were assembled, followed by electrochemical impedance spectroscopy (EIS) measurements after various resting times. The Nyquist plots (Fig. 1b and Fig. S3a, ESI†) and fitted resistance values (Fig. S3b and Table S1, ESI†) show that the LiSn|LiSn cell initially exhibits a total resistance (R_t) of 24.3 Ω. This resistance gradually decreases as the resting time extends to 10 h, indicating the formation of a favorable electrode–electrolyte interface. With further resting, R_t slightly increases and then stabilizes, suggesting that side reactions are effectively suppressed and an ultra-stable LiSn–LPSC interface is established. In contrast, the Li|Li cell exhibits a significantly higher initial R_t of 46.5 Ω. Although this resistance decreases slightly after 5 h of resting, it then continuously increases with extended resting time (Fig. 1c and Fig. S3c, d and Table S1, ESI†), indicating poor interfacial stability and ongoing side reactions at the Li–LPSC interface. These findings are consistent with the AIMD results, further confirming the superior compatibility of the Li–Sn alloy with LPSC.

The stability of the LiSn–LPSC interface was further validated through galvanostatic Li plating/stripping tests on a LiSn|LiSn symmetric cell. As shown in Fig. 2a and Fig. S4 (ESI†), when the current density increases from 0.1 (10 h) to 0.5 (10 h) to 1 mA cm^{-2} (subsequent cycling), the corresponding overpotential rises from 72 to 334 to 470 mV. Notably, the cell remains stable for over 1100 h at 1 mA cm^{-2} and 1 mA h cm^{-2} without a significant increase in overpotential. In contrast, the Li|Li symmetric cell can only operate at 0.1 mA cm^{-2} and 0.1 mA h cm^{-2}, showing a continuous increase in overpotential and ultimately failing after 130 h of cycling (Fig. S5a, ESI†), further indicating the poor stability of the Li–LPSC interface.

EIS measurements were conducted at different cycling stages to assess interfacial stability (Fig. 2b and Fig. S5b, Table S2, ESI†). The R_t of the LiSn|LiSn cell initially decreases during the first 20 h of cycling, followed by a slight increase as cycling extends to 200 h. This trend mirrors the behavior observed during resting, further confirming the formation of a stable LiSn–LPSC interface in the cycled LiSn|LiSn cell.

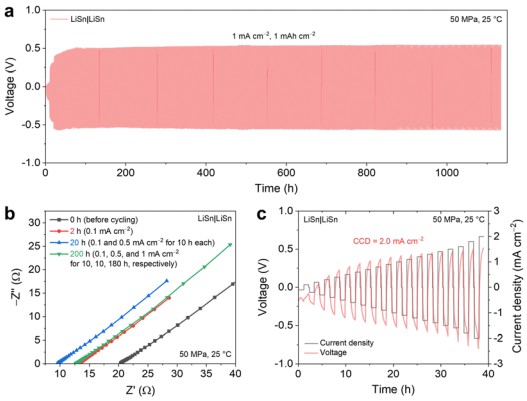

Fig. 2 Voltage profiles (a), EIS spectra after cycling (b), and CCD testing (c) of LiSn|LiSn cell.

The critical current density (CCD), which represents the maximum current density a cell can withstand before short-circuiting due to Li dendrite penetration,[13] was also evaluated. As shown in Fig. 2c, the CCD of the LiSn|LiSn cell was determined by gradually increasing the current density with a fixed Li plating/stripping time of 1 h. The overpotential progressively increases with rising current density, and the cell short-circuits at 2.0 mA cm^{-2}, indicating its CCD. This value is not only significantly higher than that of the Li|Li cell (0.7 mA cm^{-2}, Fig. S5c, ESI†) but also exceeds those of symmetric cells with modified Li metal electrodes (Table S3, ESI†).[14] These results demonstrate that the LiSn electrode exhibits excellent high-rate capability and strong dendrite suppression ability.

To evaluate the practical application of Sn- and Li-based anodes, full cells with LPSC SE were assembled, including LiSn|NCM811, Sn|NCM811, and Li|NCM811 configurations. Fig. 3a presents the initial galvanostatic charge–discharge profiles at a rate of 0.1C (1C = 200 mA g^{-1}) with a cathode active material (CAM) loading of 12.74 mg cm^{-2}. As expected, the LiSn|NCM811 cell exhibits the highest specific capacity (163 mA h g^{-1}) and initial CE of 75%, outperforming the Sn-based (106 mA h g^{-1}, 52%) and Li-based (119 mA h g^{-1}, 73%) cells. The inferior performance of Sn|NCM811 and Li|NCM811 cells is attributed to Li loss—caused by solid electrolyte interphase formation and irreversible Li trapping in the Sn anode—and the poor stability of the Li–LPSC interface, respectively.[15] Additionally, the optimal prelithiation content of the Sn anode was investigated (Fig. S6, ESI†). As the Li content decreases from LiSn to $Li_{0.75}Sn$ to $Li_{0.5}Sn$, the corresponding full

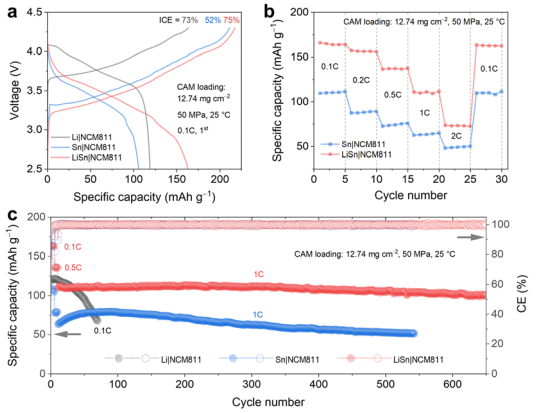

Fig. 3 Electrochemical performance of NCM811-based full cells with Li, LiSn, and Sn anodes. (a) Voltage profiles, (b) rate capability, and (c) cycling stability.

cells exhibit progressively lower specific capacities and initial CE values, indicating that sufficient prelithiation is essential to compensate for Li loss during cycling.

The rate performance of LiSn|NCM811 and Sn|NCM811 full cells was evaluated. As shown in Fig. 3b and Fig. S7 (ESI†), the LiSn|NCM811 cell delivers specific capacities of 165, 157, 137, 111, 74, and 163 mA h g^{-1} at rates of 0.1C, 0.2C, 0.5C, 1C, 2C, and back to 0.1C, respectively—significantly outperforming the Sn|NCM811 cell. Furthermore, the long-term cycling stability of the full cells was assessed (Fig. 3c and Fig. S8, S9, ESI†). The Sn-based cells were cycled at 0.1C for 5 cycles, followed by 0.5C for 5 cycles, and then 1C for the remaining cycles, while the Li|NCM811 cell was cycled at 0.1C throughout. The LiSn|NCM811 cell demonstrates remarkable cycling stability, retaining 91% of its capacity after 650 cycles (Table S4, ESI†). In comparison, the Sn|NCM811 cell exhibits moderate stability, with 81% capacity retention after 540 cycles, whereas the Li|NCM811 cell suffers from continuous capacity decay, retaining only 57% of its capacity after 70 cycles. These results further confirm the excellent compatibility between the Li–Sn alloy and LPSC and highlight the poor stability of the Li–LPSC interface.

To investigate the performance differences between LiSn|NCM811 and Sn|NCM811 cells, EIS measurements and real-time uniaxial pressure change (Δp) monitoring were conducted.[16] The Nyquist plots (Fig. S10, ESI†) and fitted resistances (Table S5, ESI†) reveal that both cells exhibit similar initial interfacial resistance (R_{int}, 17.2 *vs.* 15.9 Ω). However, after 50 cycles, the LiSn-based cell maintains a lower R_{int} (37.7 *vs.* 56.6 Ω), indicating the formation of a more stable anode–SE interface. Real-time Δp monitoring was used to assess the volume changes of the anodes, considering that NCM811 and LPSC SE exhibit negligible volume fluctuations during cycling. The voltage profiles and corresponding Δp curves of the LiSn|NCM811 and Sn|NCM811 cells (Fig. S11, ESI†) show that both experience an increase in Δp during charging—corresponding to anode expansion—followed by a decrease during discharging due to contraction. The LiSn|NCM811 cell exhibits an average maximum Δp of 0.17 MPa over the first three cycles, which is lower than that of the Sn|NCM811 cell (0.23 MPa) and reported Si-based full cells. These results indicate that prelithiation effectively mitigates the volume change of the Sn anode, leading to a more stable anode–SE interface and improved electrochemical performance.

CAM mass loading is a critical parameter for determining the energy density of full cells.[17] The electrochemical performance of Sn-based full cells with a high CAM loading of 38.22 mg cm^{-2} was evaluated (Fig. S12, ESI†). At 0.1C, the LiSn|NCM811 cell delivers a higher areal capacity (5.3 mA h cm^{-2}) compared to the Sn|NCM811 cell (3.5 mA h cm^{-2}). Furthermore, the LiSn-based cell maintains an areal capacity of 4.2 and 3.8 mA h cm^{-2} at 0.5C and 1C, respectively, and retains 100% of its capacity after 100 cycles at 1C. In contrast, the Sn|NCM811 cell delivers significantly lower areal capacities of 1.6 and 0.7 mA h cm^{-2} at 0.5C and 1C, respectively. These results suggest that the detrimental effect of anode volume expansion is exacerbated in high-CAM-loading full cells.

To gain deeper insight into the evolution of the LiSn–LPSC interface during cycling, *in situ* Raman spectroscopy was performed on a customized LiSn|NCM811 cell. The laser beam was focused on the LiSn–LPSC interface (Fig. S13, ESI†). In the initial Raman spectrum collected before charging, characteristic peaks corresponding to PS_4^{3-} (415 cm^{-1}) and Li_2S (375 cm^{-1}) were observed, indicating that interface evolution occurs upon contact between LiSn and LPSC (Fig. S14, ESI†).[18] Throughout subsequent charging and discharging cycles, the Raman spectra remained consistent with the initial spectrum, with no new peaks appearing or significant intensity reductions observed. This suggests that a stable and favorable interface forms rapidly.

The composition of the anode interface was further analyzed *via* X-ray photoelectron spectroscopy (XPS) on pristine and cycled LiSn anodes (after 50 cycles). In the Sn 3d XPS spectrum of pristine LiSn (Fig. S15a, ESI†), two fitted $3d_{5/2}$ peaks at 483.3 eV and 485.1 eV were assigned to the $Li_{22}Sn_5$ alloy and metallic Sn^0, respectively.[19] After cycling, the LiSn anode exhibited a single $3d_{5/2}$ peak at 484.5 eV (Fig. S15b, ESI†), corresponding to the Li_xSn ($0 < x < 4.4$) alloy, indicating complete alloying of Sn and strong interfacial stability between the Sn/LiSn anode and LPSC SE. Additionally, the S 2p XPS spectra of the anodes (Fig. S15c and d, ESI†) revealed that the cycled LiSn anode exhibited an additional $2p_{3/2}$ peak at 160.3 eV, attributed to Li_2S, alongside the original PS_4^{3-} peak at 161.6 eV.[3] These results confirm the formation of a stable, Li_2S-enriched LiSn–LPSC interphase during cycling.

The volumetric changes of Sn-based anodes during cycling were investigated using *ex situ* cross-sectional scanning electron microscopy (SEM). As shown in Fig. 4, the pristine LiSn anode had an initial thickness of ~25 μm, which increased to ~57 μm after the first charging, corresponding to a 128% volume expansion. During subsequent discharging, the anode thickness slightly decreased, and a porous structure was observed, indicating uniform delithiation and high mechanical stability of the dealloyed anode. After 50 cycles, the cycled LiSn anode retained a thickness of ~64 μm, demonstrating excellent structural stability. In contrast, the pristine Sn anode expanded significantly from ~25 μm to ~76 μm after charging (Fig. S16, ESI†), corresponding to a large volume expansion of 204%. After 50 cycles, the Sn anode exhibited

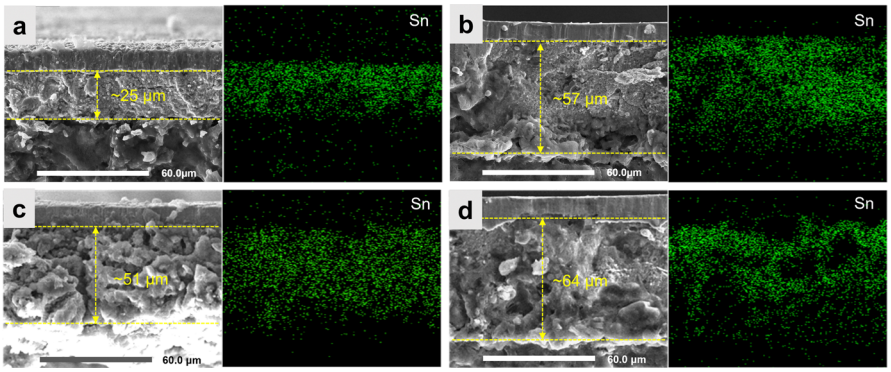

Fig. 4 Thickness of LiSn anodes under different states. (a) Initial, (b) charging, (c) discharging, and (d) after 50 cycles.

a thickness of ~95 μm, highlighting its poor structural stability compared to LiSn. It is worth noting that the unique non-compact structure also helps to alleviate volume expansion of the as-prepared anodes during lithiation (Fig. S17, ESI†).

In conclusion, a prelithiated Sn anode was successfully prepared and employed in LPSC-based ASSLBs, following AIMD simulations that confirmed its high stability with LPSC. As expected, the LiSn|NCM811 cell exhibited superior specific capacity and extended cycling lifespan compared to Sn- and LMA-based full cells. *In situ* Raman spectroscopy and *ex situ* XPS analyses revealed the formation of an ultra-stable, Li_2S-enriched interphase at the LiSn–LPSC interface. Additionally, *in situ* Δp monitoring and *ex situ* cross-sectional SEM imaging confirmed that the LiSn anode undergoes significantly less volume change during cycling than the Sn anode. The combination of a stable interfacial structure and reduced volume fluctuation accounts for the outstanding stability of the as-prepared LiSn anode.

This work was financially supported by the National Natural Science Foundation of China (52102091, 52173205) and Guangdong Provincial University Innovation Team Project (2023KCXTD038). The computations in this paper were run on the π 2.0 cluster supported by the Center for High Performance Computing at Shanghai Jiao Tong University (SJTU). We thank the support from the Instrumental Analysis Center of SJTU.

Data availability

The data supporting this article have been included as part of the ESI.†

Conflicts of interest

There are no conflicts to declare.

Notes and references

1 Q. Zhao, S. Stalin, C.-Z. Zhao and L. A. Archer, *Nat. Rev. Mater.*, 2020, **5**, 229–252.
2 C. Wang, J. Liang, Y. Zhao, M. Zheng, X. Li and X. Sun, *Energy Environ. Sci.*, 2021, **14**, 2577–2619.
3 Y. L. Wu, R. Z. Zhang, Q. J. Huang, J. J. Wang, K. Y. Jiang, Z. Y. Chen, J. H. Zhu and X. D. Zhuang, *Chem. Commun.*, 2024, **60**, 13578–13581.
4 G. H. Zhang, Z. H. Yang and Y. Ma, *Acta Chim. Sin.*, 2023, **81**, 1387–1393.
5 L. Ye, D. Wang, Q. Lu, L. J. Jhang, R. Kou, A. K. Pandey, J. Lira, M. Liao and D. Wang, *Adv. Mater.*, 2024, **36**, 2407724.
6 J. Li, J. Luo, X. Li, Y. Fu, J. Zhu and X. Zhuang, *EcoMat*, 2023, **5**, e12383.
7 D. H. S. Tan, Y. T. Chen, H. Yang, W. Bao, B. Sreenarayanan, J. M. Doux, W. Li, B. Lu, S. Y. Ham, B. Sayahpour, J. Scharf, E. A. Wu, G. Deysher, H. E. Han, H. J. Hah, H. Jeong, J. B. Lee, Z. Chen and Y. S. Meng, *Science*, 2021, **373**, 1494–1499.
8 W. Yan, Z. Mu, Z. Wang, Y. Huang, D. Wu, P. Lu, J. Lu, J. Xu, Y. Wu, T. Ma, M. Yang, X. Zhu, Y. Xia, S. Shi, L. Chen, H. Li and F. Wu, *Nat. Energy*, 2023, **8**, 800–813.
9 Y. Tian, Z. Pei, D. Luan and X. W. Lou, *Angew. Chem., Int. Ed.*, 2025, **64**, e202423454.
10 J. Zhu, J. Luo, J. Li, S. Huang, H. Geng, Z. Chen, L. Jia, Y. Fu, X. Zhang and X. Zhuang, *Adv. Mater.*, 2024, **36**, 2407128.
11 S.-Y. Ham, E. Sebti, A. Cronk, T. Pennebaker, G. Deysher, Y.-T. Chen, J. A. S. Oh, J. B. Lee, M. S. Song, P. Ridley, D. H. S. Tan, R. J. Clément, J. Jang and Y. S. Meng, *Nat. Commun.*, 2024, **15**, 2991.
12 S. Luo, X. Liu, X. Zhang, X. Wang, Z. Wang, Y. Zhang, H. Wang, W. Ma, L. Zhu and X. Zhang, *ACS Energy Lett.*, 2022, **7**, 3064–3071.
13 S.-Y. Ham, H. Yang, O. Nunez-cuacuas, D. H. S. Tan, Y.-T. Chen, G. Deysher, A. Cronk, P. Ridley, J.-M. Doux, E. A. Wu, J. Jang and Y. S. Meng, *Energy Storage Mater.*, 2023, **55**, 455–462.
14 H. Wan, Z. Wang, W. Zhang, X. He and C. Wang, *Nature*, 2023, **623**, 739–744.
15 Y.-H. Lee, D.-H. Kim, J.-M. Yoon, I.-C. Choi, J.-H. Choi, K.-J. Jeon, Y.-C. Ha and C.-M. Park, *Joule*, 2024, **8**, 2777–2793.
16 S. Y. Han, C. Lee, J. A. Lewis, D. Yeh, Y. Liu, H.-W. Lee and M. T. McDowell, *Joule*, 2021, **5**, 2450–2465.
17 Y. Li, S. Song, H. Kim, K. Nomoto, H. Kim, X. Sun, S. Hori, K. Suzuki, N. Matsui, M. Hirayama, T. Mizoguchi, T. Saito, T. Kamiyama and R. Kanno, *Science*, 2023, **381**, 50–53.
18 R. Zhang, Y. Wu, Z. Chen, Y. Wang, J. Zhu and X. Zhuang, *J. Mater. Chem. A*, 2023, **11**, 19195–19209.
19 X. You, N. Chen, G. Xie, S. Xu, S. Y. Sayed and L. Sang, *ACS Appl. Mater. Interfaces*, 2024, **16**, 35761–35770.

